



NiCoCr-based medium-entropy alloys with superior resistance to radiation hardening and helium cavity growth



Shaofei Liu^{a,b}, Guma Yeli^{c,*}, Da Chen^d, Weitong Lin^a, Yilu Zhao^e, Junhua Luan^f, Shijun Zhao^a, Tao Yang^f, Ji-jung Kai^{a,b,*}

^a Department of Mechanical Engineering, City University of Hong Kong, Hong Kong, China

^b Center for Advanced Nuclear Safety and Sustainable Development, City University of Hong Kong, Hong Kong, China

^c Institute of Nuclear and New Energy Technology, Tsinghua University, Beijing, China

^d School of Energy and Environment, Southeast University, Nanjing, China

^e School of Materials Science and Engineering, Harbin Institute of Technology, Shenzhen, China

^f Department of Materials Science and Engineering, City University of Hong Kong, China

ARTICLE INFO

Article history:

Received 25 July 2022

Revised 16 November 2022

Accepted 10 December 2022

Available online 11 December 2022

Keywords:

Medium-entropy alloy

Radiation hardening

He cavity

NiCoCr

ABSTRACT

In this work, three NiCoCr-based medium-entropy alloys (MEAs), i.e., NiCoCr, NiCoCrW_{0.1} and NiCoCrTi_{0.1}, were irradiated with helium (He) ions at 400 °C and 700 °C to study the radiation hardening and He-induced cavity growth behavior. The typical quaternary FeCoNiCr alloy was irradiated similarly and evaluated for comparison. Using transmission electron microscopy and nanoindentation measurements, He-induced microstructural evolution and mechanical changes were systematically investigated. Here we show that mitigated radiation hardening at 400 °C and cavity growth behavior at 700 °C were exhibited in the NiCoCr-based MEAs, in contrast to significant radiation hardening and He cavity growth of FeCoNiCr. Among the studied alloys, NiCoCrW_{0.1} displayed the best radiation hardening resistance, while NiCoCrTi_{0.1} presented the strongest tolerance in terms of He cavity growth. The underlying reasons were carefully analyzed based on the observed microstructures. Our results demonstrate the great potential of NiCoCr-based MEAs to function as critical nuclear structural components at relatively low and high temperatures.

© 2022 Elsevier B.V. All rights reserved.

1. Introduction

The last decade has seen the emergence of an intriguing class of materials, i.e., high-entropy alloys (HEAs) or medium-entropy alloys (MEAs). Unlike the traditional alloy design concept, HEAs/MEAs composed of multiple principal elements intriguingly exhibit a variety of excellent performances [1–8]. Recently, extensive research has demonstrated that the distinctive compositional complexity and severe lattice distortion grant HEAs/MEAs superior irradiation resistance, making them potential candidates for advanced nuclear reactor systems [7–12]. Previous studies have demonstrated that the void swelling tolerance of HEAs subjected to heavy ions irradiation can be influenced by adjusting the elemental constituent types or numbers. For instance, Lu et al. [7] reported that increasing elemental component numbers of HEAs can effectively suppress void swelling by regulating defect migration mode and subsequently enhancing defect recombination. The results re-

vealed that the equiatomic FeCoNiCrMn HEA only exhibited a void swelling value of as small as ~0.1% when irradiated by Ni ions at 500 °C, which is significantly superior to pure Ni (~9.4%).

In addition to void swelling, structural materials may be up against various challenges at different temperature regimes. In general, void swelling typically follows a bell-shaped curve between 0.3~0.6 T_m (T_m: absolute melting temperature), and the peak swelling usually occurs at an intermediate temperature [13]. At low temperatures (< 0.4 T_m), void growth is suppressed due to deficient mobility of vacancies [13,14]. In this case, radiation-induced hardening arising from sessile defects like dislocation loops and helium (He) bubbles may pose a threat to structural materials due to the detrimental effect on the work hardening capacity [14,15]. Previous studies showed that during irradiation, the FeCoNiCrMn HEA displayed a larger hardening effect compared to its derivatives due to the formation of high-density He bubbles and dislocation loops [11,16]. At high temperatures (> 0.5T_m), void growth is also restrained owing to the loss of vacancy supersaturation [13,17]. Instead, volumetric swelling and surface blistering will become a big concern due to He bubble growth and agglomeration [18]. Our previous results demonstrated that FeCoNiCrMn showed

* Corresponding authors.

E-mail addresses: ylgm@tsinghua.edu.cn (G. Yeli), jijkai@cityu.edu.hk (J.-j. Kai).

superior He bubble growth resistance at low temperatures, while it displayed significant temperature sensitivity on account of the low melting temperature and exhibited extremely poor He-induced cavity growth tolerance even worse than pure Ni at 700 °C [10]. Therefore, HEAs with high compositional complexity may be less competitive for nuclear structural components at relatively low and high temperatures.

Considering the extensive He production via transmutation reaction (n, α) in the future fast reactors and D-T reaction in the proposed fusion reactors [15,19], it is pivotal to develop novel HEAs/MEAs with desired He-induced hardening and volumetric swelling tolerance for key structural components. It has been reported that alloys with lower compositional complexity displayed stronger radiation hardening resistance due to the formation of less sessile faulted dislocation loops [11]. Meanwhile, our previous results revealed that at high temperatures, decreasing compositional complexity tends to restrain vacancy migration toward He cavities and then suppress He cavity growth [10]. Among the derivatives with relatively low compositional complexity of the Fe-CoNiCrMn HEA, NiCoCr stands out due to the excellent synergy of strength and ductility, which is even superior to FeCoNiCrMn and 316 L stainless steel [20]. It is therefore reasonable to expect that NiCoCr can be a suitable base alloy to develop novel alloys with both superior He-induced hardening and cavity growth resistance. Unfortunately, limited endeavors have been made in the radiation behavior of NiCoCr because of its inferior void swelling resistance at intermediate temperatures [9], even though it shows great potential to be utilized as critical nuclear components at low and high temperatures.

In the current study, the NiCoCr MEA and two minor alloyed ones, i.e., NiCoCrW_{0.1} and NiCoCrTi_{0.1}, were irradiated by He ions at 400 °C and 700 °C to investigate the He-induced hardening and He cavity growth resistance of NiCoCr-based MEAs, respectively. Additionally, the typical FeCoNiCr HEA with a higher degree of compositional complexity was also selected as a reference sample. The radiation-induced microstructure evolution in the studied materials was comparatively characterized by transmission electron microscopy (TEM). Nanoindentation was utilized to investigate the radiation-induced hardening effects of the alloys. The underlying mechanisms responsible for the He-induced hardening and cavity growth behavior were carefully explored.

2. Experimental

Ingots of the studied alloys, i.e., FeCoNiCr, NiCoCr, NiCoCrW_{0.1} and NiCoCrTi_{0.1}, were prepared using high purity (> 99.9%) raw metals by arc melting under a high-purity protective argon atmosphere and then solidified in a water-cooled copper mold. Before irradiation, the alloys were homogenized for 2 h at 1200 °C followed by water quenching to ensure homogeneity. Subsequently, one surface of each sample was mechanically polished with silicon carbide paper down to a 4000-grit SiC paper. Then the samples were electrochemically polished with a solution of C₂H₆O and HNO₃ in a 4:1 ratio at 30 V and ambient temperature to remove surface stress. The surface microstructure and chemical composition of the alloys before irradiation were examined by a Zeiss Supra55 scanning electron microscopy (SEM) equipped with energy-dispersive spectrometry (EDS).

The samples were irradiated with 275 keV He⁺ ions at 400 °C and 700 °C to a fluence of $6.4 \times 10^{20} m^{-2}$ in the Accelerator Laboratory at National Tsing Hua University. The irradiation flux was controlled at about $4.5 \times 10^{12} cm^{-2} s^{-1}$. Ion-induced damage and injected He concentration as a function of implantation depth were calculated using SRIM-2013 in the quick Kinchin-Pease option [21], as shown in Fig. 1. The displacement threshold energies for all the

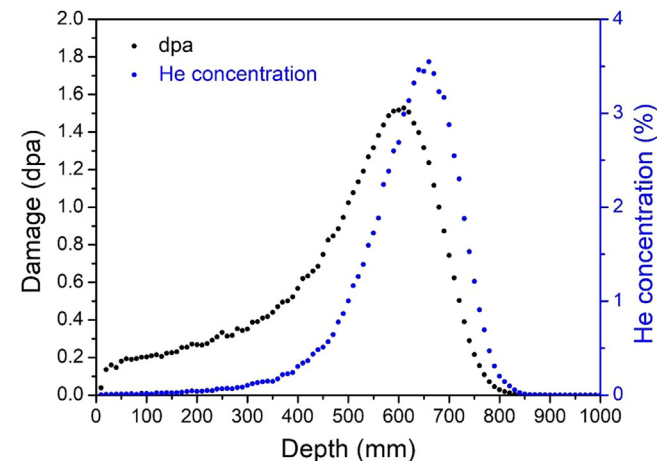


Fig. 1. Damage and He concentration profiles as a function of implantation depth predicted by SRIM.

elemental constituents were set to be 40 eV. Due to the similar densities of the studied alloys, there is little difference in the SRIM prediction. The peak irradiation depth of the He concentration is ~700 nm, whereas that of dpa is ~600 nm.

Hardness measurements on the unirradiated and 400 °C-irradiated alloys were conducted at room temperature using MTS DSM nanoindenter which was calibrated against a fused silica standard sample. A Berkovich-type indentation tip was used with the continuous stiffness measurement mode to measure the hardness along indenter depth. Indents were produced in a direction normal to the sample surface. A minimum of 8 indents approximately 50 μm apart from each other were obtained at the same depth on each specimen to get an average hardness value to ensure statistical accuracy.

To study the He-induced defects, cross-sectional transmission electron microscopy (TEM) samples from the irradiated alloys were fabricated by the focused ion beam (FIB) lift-out technique using an FEI Scios Dual-Beam system. Bright-field (BF) images of irradiation-induced defects were captured using a JEM-2100F TEM operated at 200 kV. He bubbles or cavities were characterized away from the zone axis with an under-focus condition, and dislocation structures were imaged with two-beam conditions near $g = (200)$. Convergent beam electron diffractions were used to measure the thicknesses of TEM samples. Besides, Shockley partial dislocations in the studied alloys were also characterized by the weak-beam dark-field (WBDF) technique in TEM to evaluate the stacking fault energy (SFE) of NiCoCrTi_{0.1} and NiCoCrW_{0.1}. Detailed methods are the same as Refs. [22,23]. In addition, atom probe tomography (APT) analysis was conducted to examine the phase stability of the NiCoCrTi_{0.1} MEA irradiated at 700 °C by using Cameca LEAP 5000XR equipment.

3. Results

3.1. Pristine microstructures

Table 1 displays the nominal chemical compositions and the actual ones analyzed by SEM-EDS of the pristine alloys. Clearly, the alloy compositions are close to the targeted ones. Prior to irradiation, the initial microstructures of the studied alloys were characterized by SEM and TEM, as shown in Fig. 2. The SEM images display the fully-recrystallization microstructure of all the studied alloys, with the absence of precipitates in the grain interior and at

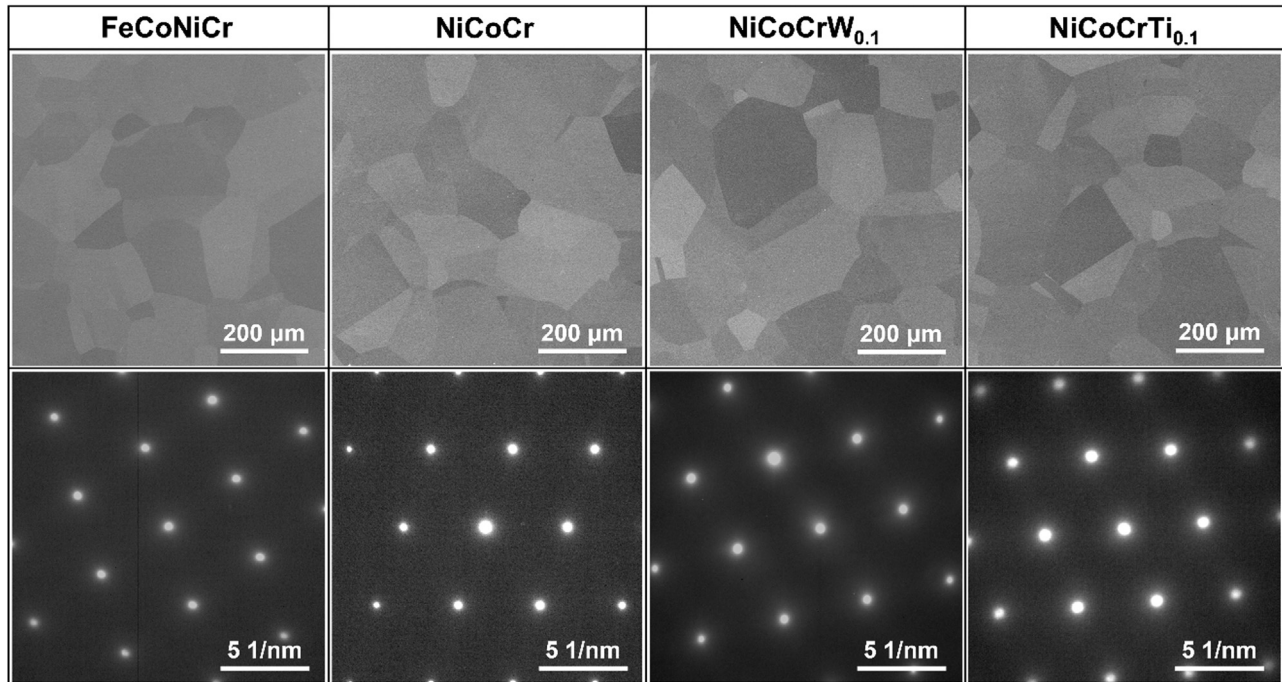


Fig. 2. SEM images and SADPs recorded at the $\langle 110 \rangle$ zone axis of the pristine alloys.

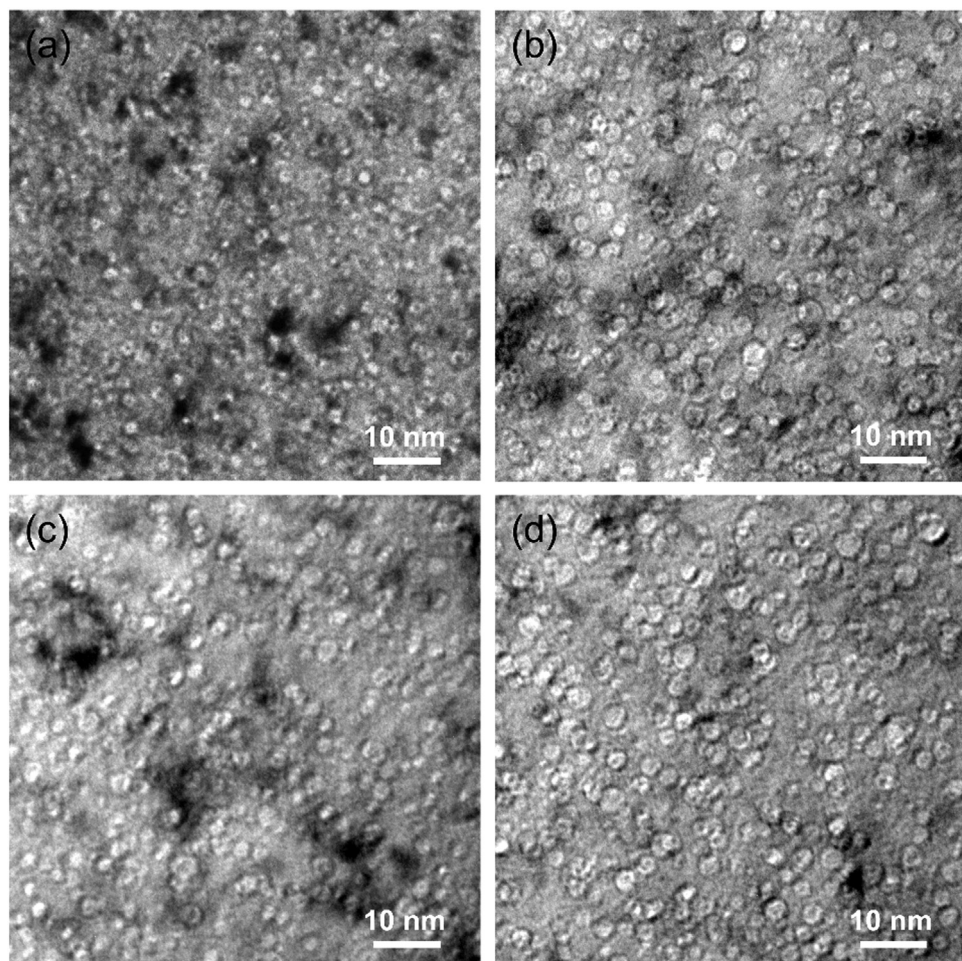


Fig. 3. BF-TEM images of He bubbles acquired from peak damaged region of (a) FeCoNiCr, (b) NiCoCr, (c) NiCoCrW_{0.1} and (d) NiCoCrTi_{0.1} irradiated at 400°C.

Table 1

Nominal and actual chemical compositions of the studied alloys (at.%).

Alloy		Fe	Co	Ni	Cr	W	Ti
FeCoNiCr	Nominal	25.00	25.00	25.00	25.00	–	–
	Actual	24.78	25.24	25.22	24.76	–	–
NiCoCr	Nominal	–	33.33	33.34	33.33	–	–
	Actual	–	33.41	33.50	33.09	–	–
NiCoCrW _{0.1}	Nominal	–	32.26	32.26	32.26	3.22	–
	Actual	–	32.12	32.43	32.14	3.31	–
NiCoCrTi _{0.1}	Nominal	–	32.26	32.26	32.26	–	3.22
	Actual	–	32.41	32.09	32.28	–	3.12

the grain boundaries. The four alloys exhibit similar average grain sizes, which are measured to be $\sim 170 \mu\text{m}$. Further analysis by selected area diffraction patterns (SADPs) acquired at the $\langle 110 \rangle$ zone axis revealed a single face-centered-cubic (FCC) crystalline structure of the four alloys.

3.2. He irradiation response at 400 °C

Fig. 3 comparatively display the He bubbles in the peak damaged region of the 400 °C-irradiated alloys under the same magnification. All the He bubbles are several nanometers in size and spherical in shape. The chemical composition significantly affects the size and density of He bubbles. Apparently, the smallest He bubbles were revealed in the FeCoNiCr alloy. Fig. 4 statistically depicts the average sizes and densities of He bubbles in the stud-

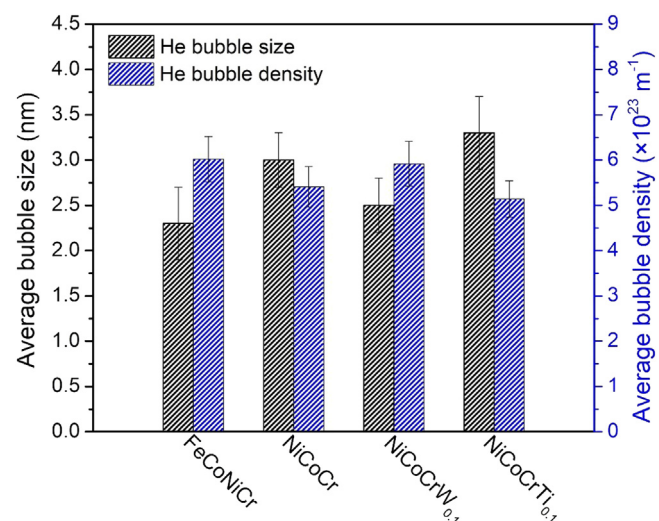


Fig. 4. Statistics for the size and number density of He bubbles at the peak damaged regions of the alloys after irradiation at 400°C.

ied alloys irradiated at 400 °C. At this temperature, the average He bubble sizes of FeCoNiCr, NiCoCr, NiCoCrW_{0.1} and NiCoCrTi_{0.1} are ~ 2.3 , ~ 3.0 , ~ 2.5 and ~ 3.3 nm, respectively. Besides, the He bubble number densities of FeCoNiCr, NiCoCr, NiCoCrW_{0.1} and NiCoCrTi_{0.1} are determined to be $\sim 6.02 \times 10^{23}$, $\sim 5.41 \times 10^{23}$, $\sim 5.92 \times 10^{23}$ and

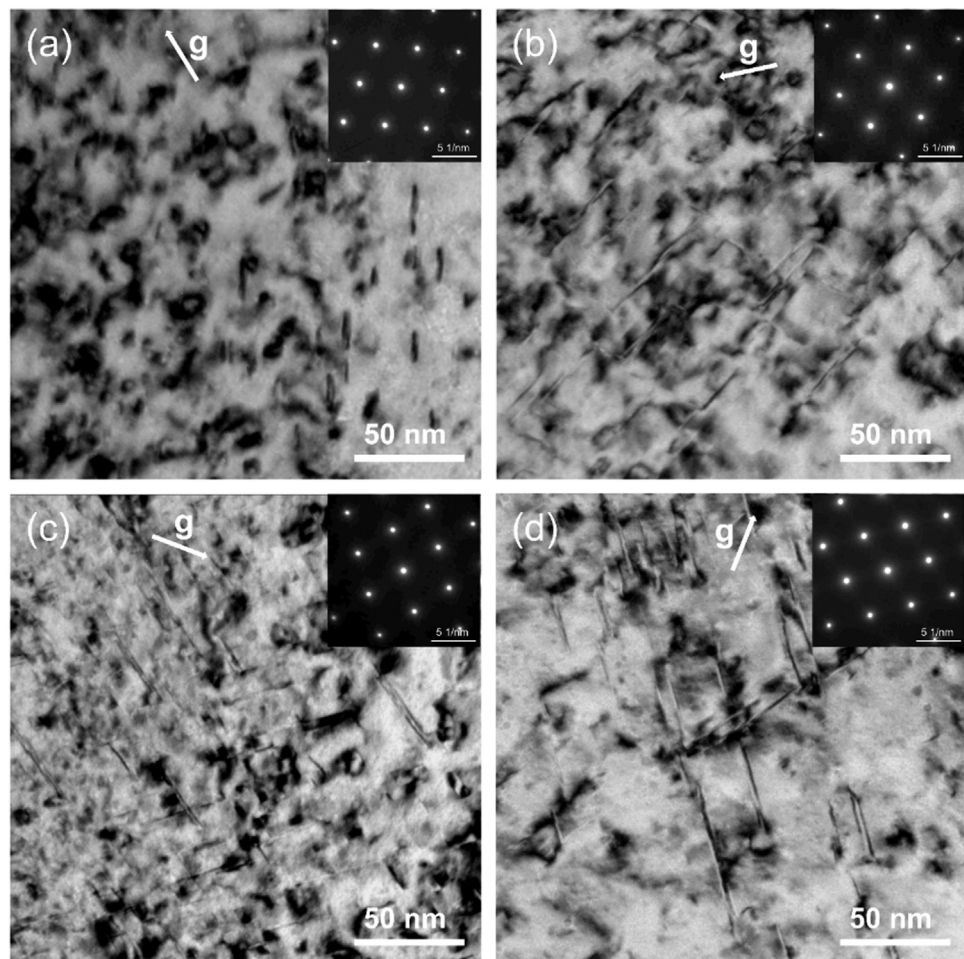


Fig. 5. BF-TEM images of irradiation-induced dislocation loops in (a) FeCoNiCr, (b) NiCoCr, (c) NiCoCrW_{0.1} and (d) NiCoCrTi_{0.1} irradiated at 400°C. The $g = (200)$ two-beam condition is marked by white arrows.

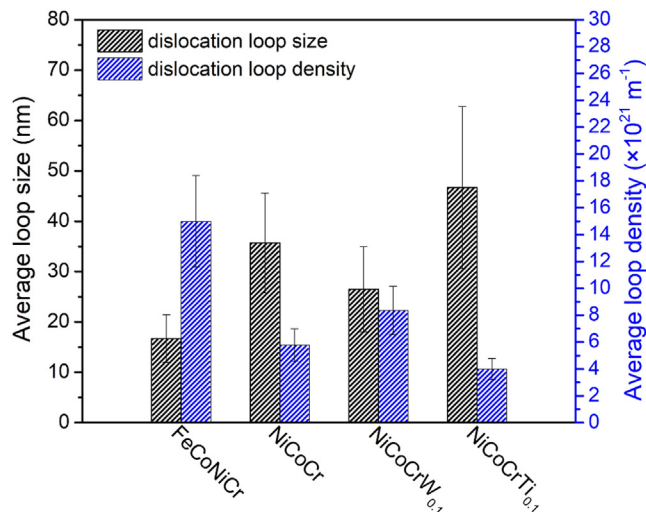


Fig. 6. Statistics for the size and number density of dislocation loops of the alloys after irradiation at 400°C.

$\sim 5.14 \times 10^{23}/\text{m}^3$, respectively. The delayed He bubble growth behavior in FeCoNiCr compared with the NiCoCr-based MEAs can be attributed to the stronger compositional complexity, which is similar to the results of previous studies [10,16,24].

The characterizations of irradiation-induced dislocation structures of the studied alloys are presented in Fig. 5. The dislocation structures were taken at a relatively low damaged region, i.e., about 200~400 nm, due to the difficulty of clear characterization of dislocation structures in the highly damaged peak region. For all the studied alloys, two sets of edge-on dislocation loops with an intersection angle of 71° were revealed, which is particularly obvious in the NiCoCr-based MEAs with larger dislocation loops. The orientations concerning the crystal direction of these dislocation loops are perpendicular to those of {111} habit planes, thus displaying the same intersection angle. The statistic results in Fig. 6 reveal that the growth of dislocation loops in the studied materials shows a similar trend to the variability of He bubbles. Compared with the NiCoCr-based MEAs, the FeCoNiCr alloy formed

dislocation loops with smaller sizes and a larger number density. The minor addition of W and Ti in the NiCoCr alloy gives rise to different dislocation loop formation behavior. After adding 3.2% W in NiCoCr, the average size of dislocation loops decreases, and the number density increases. By contrast, dislocation loops with increased size and decreased number density can be observed in the Ti-alloyed NiCoCr MEA.

3.3. Radiation-induced hardening

Figs. 7a-7d shows the average nanoindentation hardness profiles with the standard deviation values of the studied alloys with and without irradiation at 400°C. The hardness data with indentation depth of less than 50 nm were neglected because of the testing artifacts. Clearly, the hardness values of all the samples decreased gradually with the increase in depth due to the indentation size effect (ISE) [25]. The hardness values of the irradiated samples are larger compared to the pristine ones, indicating He irradiation-induced hardening of the alloys.

A model developed by Nix and Gao was applied to determine the hardness of samples with and without irradiation, in which the depth dependence of hardness can be described as follows [25]:

$$H = H_0 \sqrt{1 + \frac{h^*}{h}} \quad (1)$$

where H is the measured hardness at a given indentation depth of h , H_0 is the hardness at infinite depth, h^* is a characteristic length associated with the types of material and indenter. Based on this model, irradiation-induced hardness can be obtained by extracting hardness data of the damage region by fitting the curve [26]. The data of hardness are plotted as H^2 verse $1/h$, as shown in Figs. 7e-7h. The hardness profile of the unirradiated samples exhibits good linearity, while the character with a rather clear bilinearity is demonstrated in the irradiated materials. Clearly, a critical indentation depth of about 175 nm is revealed to be the inflection point. Beyond this critical depth, evident substrate soft effect (SSE) will influence the hardness due to that the plastic deformation will be triggered on the softer unirradiated region before the indenter tips reach the substrate. The stress-affected zone of the indenter is a hemispherical shape with a radius of 4–10 times the indentation depth [27]. In the current study, the critical indentation depth is

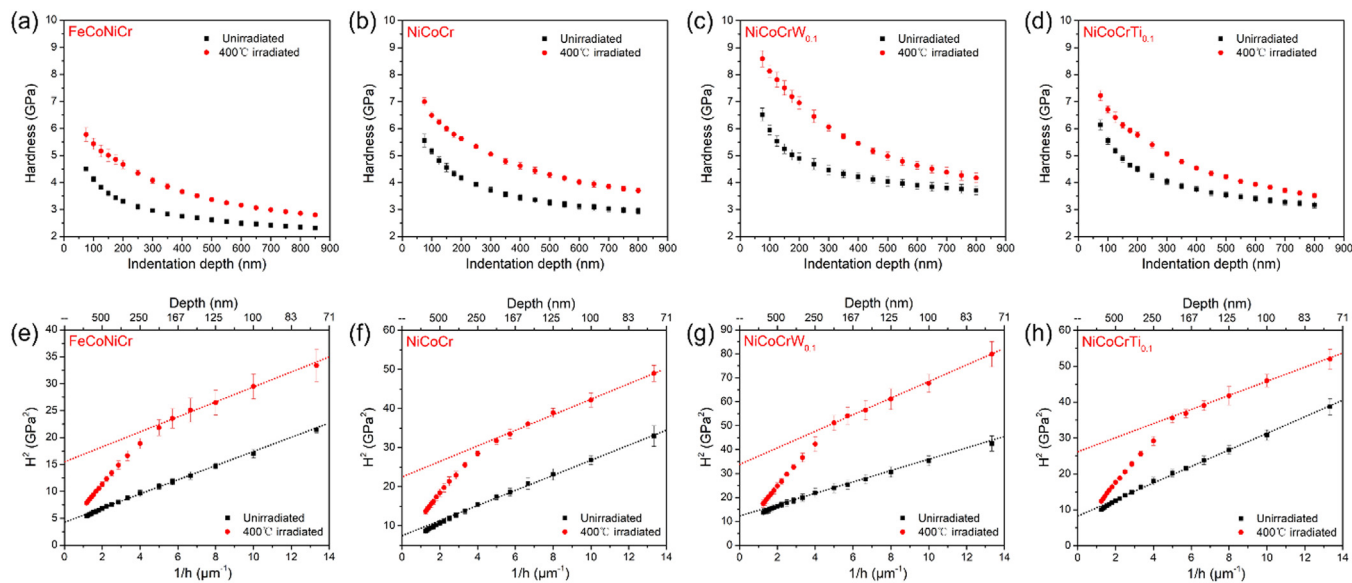


Fig. 7. (a-d) Average nanoindentation hardness as a function of indentation depth in unirradiated and 400°C-irradiated FeCoNiCr, NiCoCr, NiCoCrW_{0.1} and NiCoCrTi_{0.1}, respectively; (e-h) Profiles of H^2 – $1/h$ for average nanoindentation hardness of unirradiated and 400°C-irradiated FeCoNiCr, NiCoCr, NiCoCrW_{0.1} and NiCoCrTi_{0.1}, respectively.

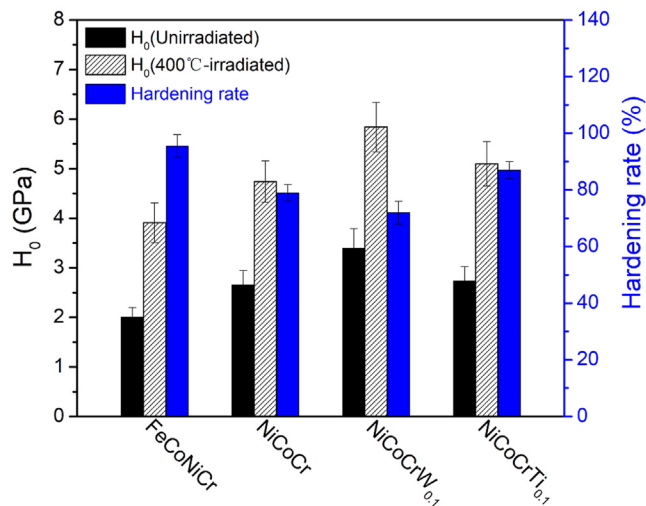


Fig. 8. Hardness values before and after irradiation at 400°C (left axis) and the degree of irradiation-induced hardening (right axis) of the studied materials.

about 1/5 of the irradiation region depth (~ 900 nm). Therefore, the hardness of the irradiation region can be well reflected by the nanoindentation test with the Berkovich diamond indenter in the current study.

In the current study, the nanohardness data points in the depth range above 75 nm of the unirradiated samples are calculated,

while those of the irradiated samples beyond the critical indentation depth ($75 \text{ nm} < h < 175 \text{ nm}$) were utilized to fitting and obtain the H_0 values, as shown in Fig. 8. Here, ΔH is defined as the difference in H_0 between the unirradiated and irradiated samples. The hardening rates of the studied samples, i.e., the ratio between ΔH and the hardness value of the pristine samples, are also plotted in Fig. 8. The result shows that compared to FeCoNiCr with an irradiation hardening value of $\sim 96\%$, NiCoCr possesses a better irradiation hardening resistance ($\sim 79\%$). This result is similar to the previous study which reported that NiCoCr displays a lower hardening rate than FeCoNiCr after being irradiated by Ni^{2+} ions at 500 °C [9]. After adding 3.2 at.% W in NiCoCr, the irradiation hardening of the alloy was slightly decreased to $\sim 72\%$. By contrast, the same amount addition of Ti in NiCoCr brings about slightly enhanced irradiation hardening behavior, as evidenced by the increment of hardening rate to $\sim 87\%$.

3.4. He irradiation response at 700°C

At 700°C, the He-induced vacancy defects in the studied alloys transformed from bubbles to cavities with large facets due to the significantly increased vacancy mobility. The BF-TEM images of He irradiation-induced cavities of the alloys irradiated at 700°C are presented in Fig. 9. At this temperature, the evolution of He-induced cavities showed a different trend with the He bubbles at 400°C. Among the four alloys, FeCoNiCr displayed the most significant temperature sensitivity in terms of He cavity growth, evidenced by the cavities with the largest average size of ~ 53.6 nm,

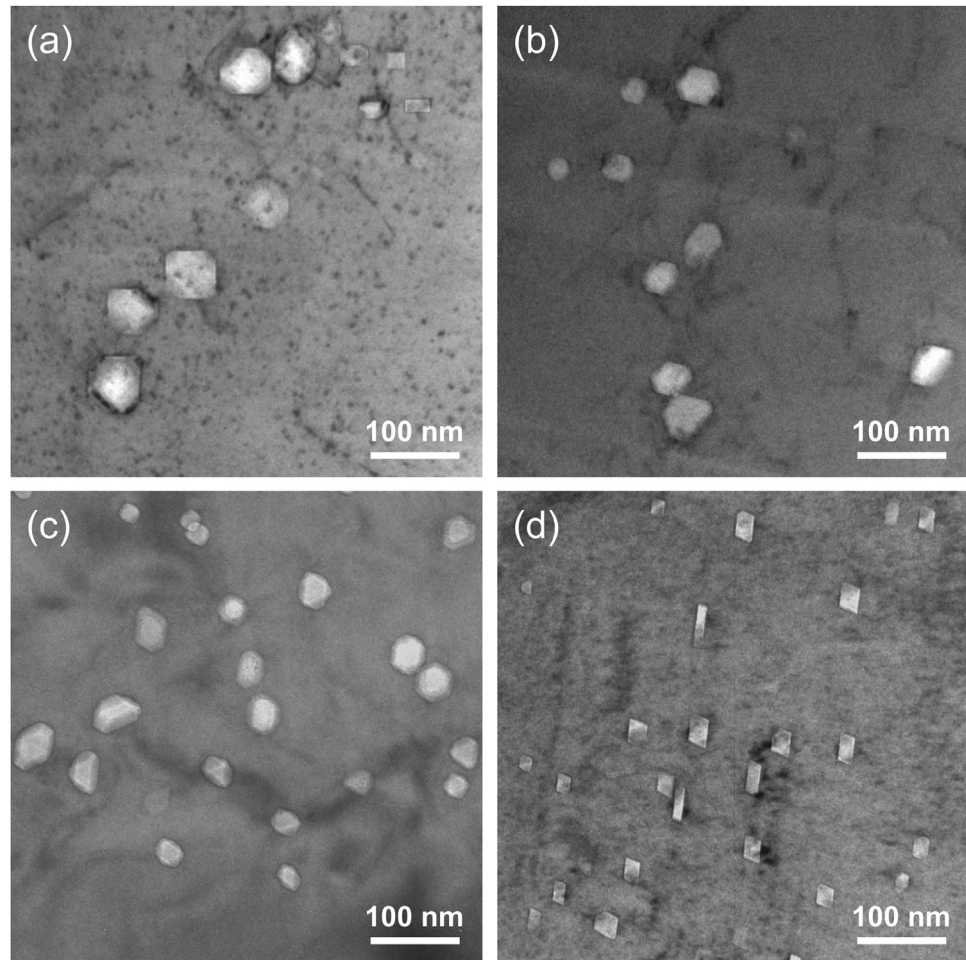


Fig. 9. The BF-TEM images of He cavities at the peak damaged regions of (a) FeCoNiCr, (b) NiCoCr, (c) NiCoCrW_{0.1} and (d) NiCoCrTi_{0.1} irradiated at 700°C.

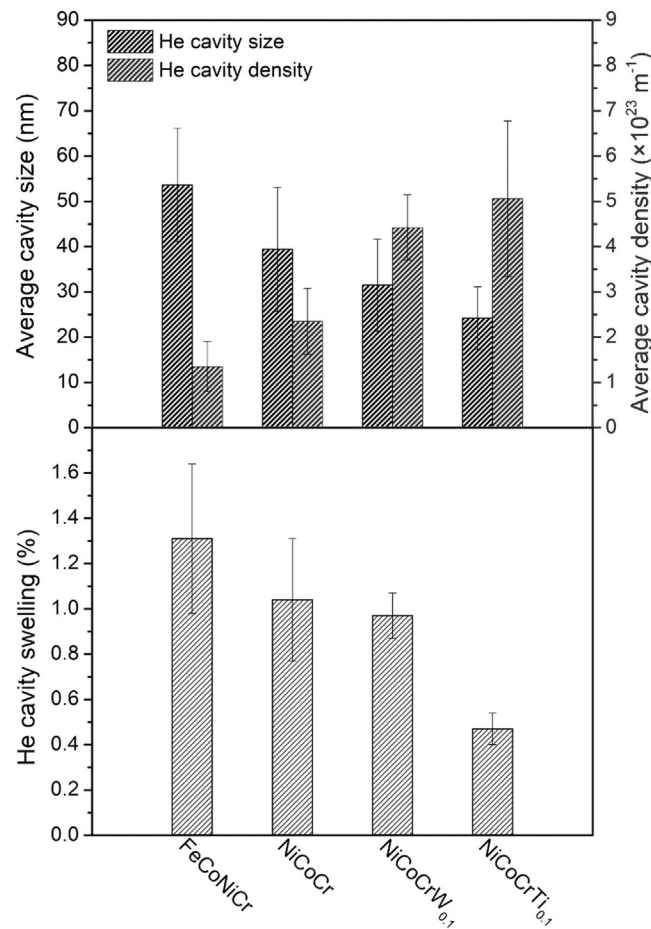


Fig. 10. Statistics for the size and number density of He cavities (top) and overall swelling (bottom) of the studied alloys irradiated at 700°C.

as shown in Fig. 9 and the statistic results in Fig. 10. Similar to that at 400°C, the minor addition of W in NiCoCr suppressed the growth of He cavities effectively and reduced their average size from ~39.4 nm to ~31.5 nm. Interestingly, the NiCoCrTi_{0.1} MEA exhibited the strongest resistance to He cavity growth among all the alloys at 700°C. The average He cavity size of the NiCoCrTi_{0.1} is determined to be ~24.2 nm, nearly half the size of FeCoNiCr. The variability of He-induced swelling at 700°C for the studied alloys is similar to the sizes of He cavities, as plotted in Fig. 10. Among the alloys, NiCoCrTi_{0.1} has the lowest swelling value (i.e., ~0.47%) in comparison with the other alloys, indicating its strongest He irradiation tolerance at high temperatures. The He cavity swelling resistance of NiCoCrTi_{0.1} is even 10 times higher than that of Fe-CoNiCrMn irradiated under the same condition [10].

With increasing temperature, the morphology of radiation-induced interstitial-type defects also changes dramatically. Fig. 11 displays the BF-TEM images of the interstitial-type defects in the studied alloys after being irradiated at 700°C. After increasing the irradiation temperature from 400°C to 700°C, dislocation loops in FeCoNiCr became thermally unstable and dissociated into long dislocation segments (Fig. 11a). By contrast, stacking fault segments with sizes of 50~200 nm dominate the radiation-induced interstitial-type defects of NiCoCr at 700°C (Fig. 11b). Meanwhile, dislocation lines and several faulted dislocation loops can also be observed. For the NiCoCrW_{0.1} MEA, dislocation lines and faulted dislocation loops with 50~140 nm in size can both be frequently observed in the peak damaged region (Fig. 11c). After being irradiated at 700°C, almost no dislocation lines and dislocation loops

were observed in the NiCoCrTi_{0.1} MEA (Fig. 11d). Instead, intersected stacking faults with sizes of submicron scale are prevalent in the damaged region. The intersected angle of 71° between the stacking faults indicates their similar nature with the dislocation loops at 400°C.

3.5. Stacking fault energies of NiCoCr-based MEAs

The formation of radiation-induced stacking fault-type defects, such as Frank loops and stacking faults, is closely associated with the SFE of alloys [13,28]. To better understand the microstructural evolution under irradiation in the studied alloys, SFE values of the NiCoCr-based MEAs were evaluated by measuring the separation distance of $a_0/6<112>$ Shockley partial dislocations. Figs. 12a and 12b show the typical WBDF images of dissociated dislocations of NiCoCrW_{0.1} and NiCoCrTi_{0.1} on the glide plane, respectively. The relationship between the SFE (γ) and dissociated distance (d) of Shockley partial dislocations can be well defined with the following equation [29]:

$$\gamma = \frac{Gb_p^2}{8\pi d} \cdot \frac{2-\nu}{1-\nu} \left(1 - \frac{2\nu \cos 2\theta}{2-\nu} \right) \quad (2)$$

where G is the shear modulus, b_p is the magnitude of Burgers vector of the $a_0/6<112>$ Shockley partials (a_0 is the lattice constant), ν is the Poisson's ratio, and θ is the total dislocation character angle. For NiCoCrW_{0.1} and NiCoCrTi_{0.1} in the current study, G and ν are determined to be 86 GPa, 0.29 and 82 GPa, 0.30 by resonant ultrasound spectroscopy, and a_0 is calculated to be 0.3579 nm and 0.3581 nm by XRD, respectively. To make sure the reliability of the obtained data, a couple of measurements were made on several different dislocations to get a standard deviation. Fig. 12c plots the measured distance d as a function of angle θ . By fitting the experimental data points with Eq. (2), the SFE values of NiCoCrW_{0.1} and NiCoCrTi_{0.1} are determined to be 19~27 (23±4) and 9~19 (14±5) mJ m^{-2} , respectively. Fig. 12d comparatively displays the SFE values of the studied four alloys. It can be seen that FeCoNiCr has the highest SFE value (i.e., 27±4 mJ m^{-2} [22]) among the four alloys. The minor alloying of W in the NiCoCr MEA gives rise to an increased SFE value, while the addition of Ti reduces the SFE of NiCoCr.

3.6. Phase stability of the irradiated alloys

To evaluate the phase stability of the studied alloys irradiated at different temperatures, the SADPs taken along the $\langle 110 \rangle$ zone axis at the peak damage region of the studied alloys in Fig. 5 and Fig. 11 were firstly examined carefully. The results reveal that the FeCoNiCr, NiCoCr and NiCoCrW_{0.1} MEAs maintain the single-FCC structure after being irradiated at both 400 °C and 700 °C, evidenced by the absence of additional reflections contributed from other phases in the SADPs. For the NiCoCrTi_{0.1} MEA, a single-FCC structure was also revealed in the 400 °C-irradiated alloy. However, after being irradiated at 700 °C, ordered superlattice diffraction spots were faintly observed, as shown in Fig. 11d. This means that an additional phase was formed in the 700 °C-irradiated NiCoCrTi_{0.1} MEA. The detailed morphology of this additional phase cannot be distinguished due to the limited resolution of our TEM. Hence, APT analysis was performed to further examine the precipitates formed in the 700 °C-irradiated NiCoCrTi_{0.1} MEA. The typical atom maps in Fig. 13a manifest that (Ni, Ti)-rich nanoprecipitates with an average size of 5.3 ± 1.5 nm are frequently distributed in the 700 °C-irradiated NiCoCrTi_{0.1} MEA. Combined with the concentration profiles in Fig. 13b and the SADP in Fig. 11d, the nanoprecipitates can be determined to be $(\text{Ni}, \text{Co}, \text{Cr})_3\text{Ti}$ -type L1₂ particles. With the assistance of the lever rule [30], the volume fraction of

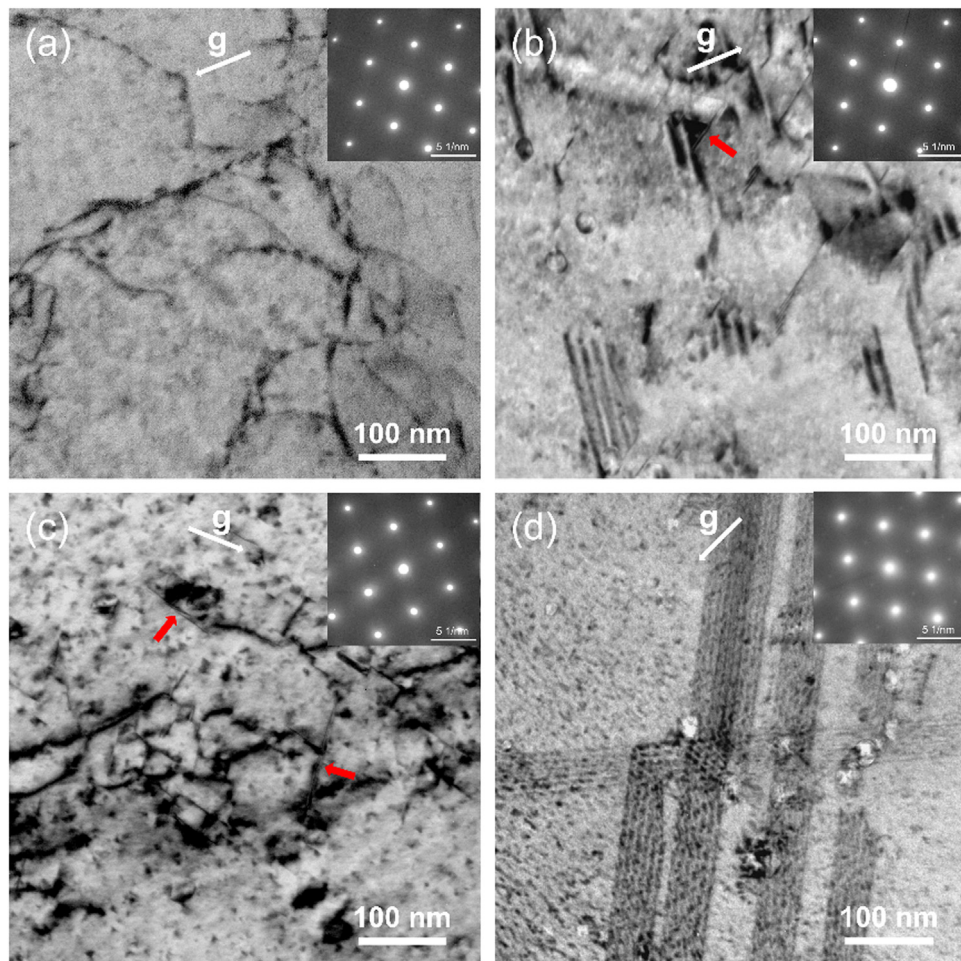


Fig. 11. BF-TEM images of irradiation-induced interstitial-type defects at the peak damaged regions of (a) FeCoNiCr, (b) NiCoCr, (c) NiCoCrW_{0.1} and (d) NiCoCrTi_{0.1} irradiated at 700°C. (The edge-on dislocation loops are marked with red arrows and the $g = (200)$ two-beam condition is marked by white arrows.).

the L₁₂ particles can be determined to be ~10.8%. These L₁₂ particles are suggested to be thermally induced precipitates due to their small lattice misfit, which is similar to previous studies [31,32]. On the other hand, the 400 °C-irradiated NiCoCrTi_{0.1} MEA may not reach equilibrium within the current irradiation period due to the slow kinetics of forming L₁₂ precipitates.

4. Discussion

At 400°C in the current work, which is around 0.4T_m for the studied alloys [33], the mobility of radiation-induced interstitial defects is relatively low while sufficient to form dislocation loops. Generally, the evolution of dislocation loops in irradiated materials could be summarized briefly in the following stages [13]. Stage I is associated with the nucleation of dislocation loops. In the initial irradiation stage, the vacancy core or the interstitial shell from the displacement cascade collapses onto a close-packed plane, leading to the formation of dislocation loops. As the temperature or dose increases, faulted dislocation loops grow up by absorbing point defects or defect clusters, corresponding to Stage II. Stage III is the thermal dissociation or coalescence of dislocation loops. As the irradiation temperature or dose continues to increase, the dislocation loops unfaulting usually occurs. The dislocation loops will eventually dissociate or coalesce into dislocation networks.

According to previous studies, the evolution of dislocation loops in HEA systems can be influenced by lattice distortion and SFE

[16,28,34]. Firstly, due to the intrinsic chemical complexity of FCC-type multicomponent alloys, the elemental constituents distribute randomly on a lattice site. Every element processes the different nearest and second-nearest neighbor atoms. Subsequently, unique site-to-site lattice distortion prevails in FCC-type multicomponent alloys, which will lead to high atomic-level stress and hinder interstitial mobility [8,35]. Therefore, the interstitial migration barrier tends to be enhanced with the increasing lattice distortion in multicomponent alloys. It will become more difficult for interstitial clusters to move when their migration energy barriers become higher, which will suppress the formation of large-sized dislocation loops. Secondly, Frank dislocation loops can be thermally stable when the following condition is satisfied [13]:

$$\gamma < \frac{Ga^2}{24\pi r} \cdot \frac{2-v}{1-v} \ln\left(\frac{2r}{r_0}\right) \quad (3)$$

where r is the radius of the Frank dislocation loop, G is the shear modulus, a is the lattice parameter, v is the Poisson's ratio, and r_0 is the dislocation core radius. Therefore, a low SFE provides energetic driving forces to improve the stability of the faulted planar defects and enable their growth to larger sizes [36].

Based on the above, it is reasonable that FeCoNiCr with severer lattice distortion and higher SFE exhibits a stronger resistance to dislocation loop growth at 400°C compared to the NiCoCr-based MEAs. A similar phenomenon was also reported by Su et al. [16] who revealed that compared to Fe₅₀Mn₃₀Co₁₀Cr₁₀ with

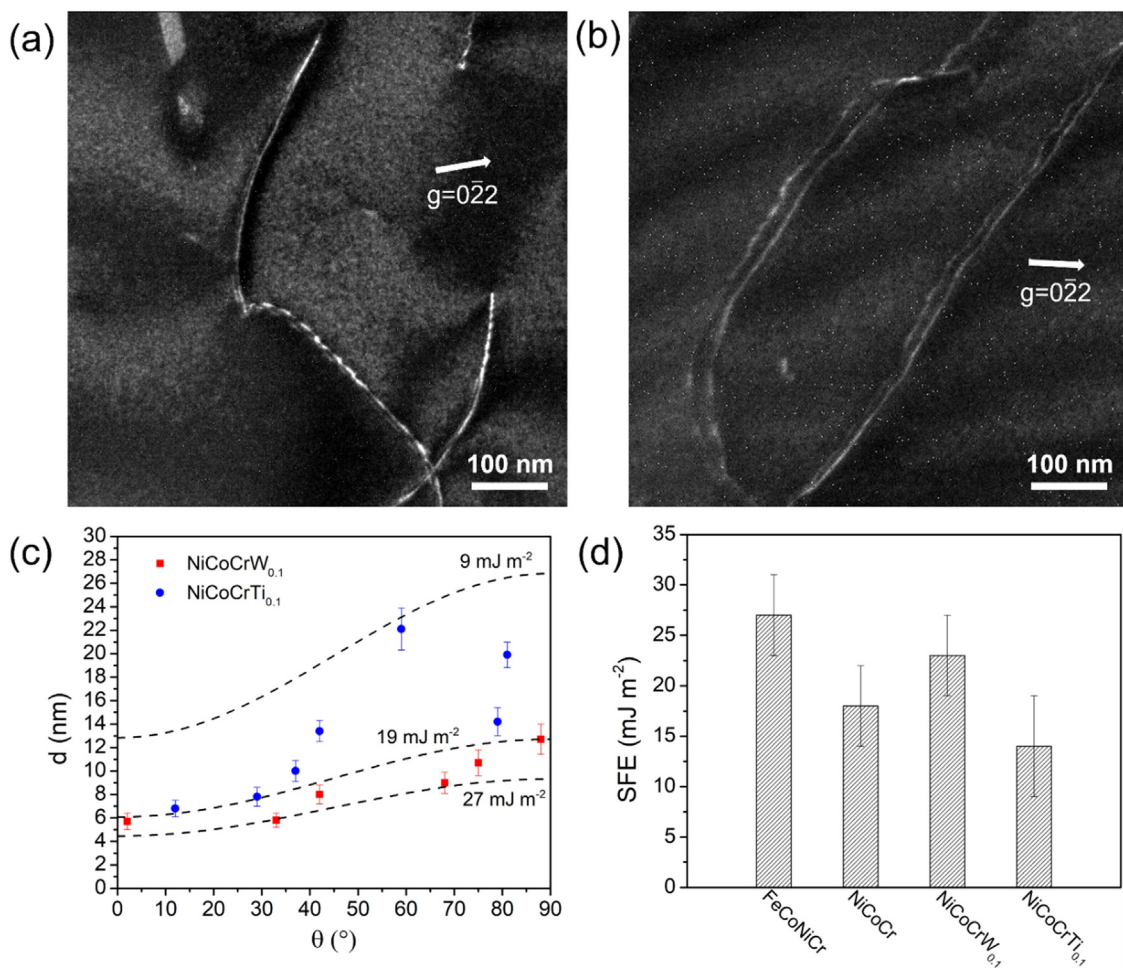


Fig. 12. The weak beam micrographs of dissociated dislocations of (a) NiCoCrW_{0.1} and (b) NiCoCrTi_{0.1}; (c) Dissociation distance of Shockley partials as a function of the total dislocation character angle; (d) Comparison of the experimentally measured SFE values of the four studied alloys (Note: the SFE values of FeCoNiCr and NiCoCr are obtained from Ref. [22]).

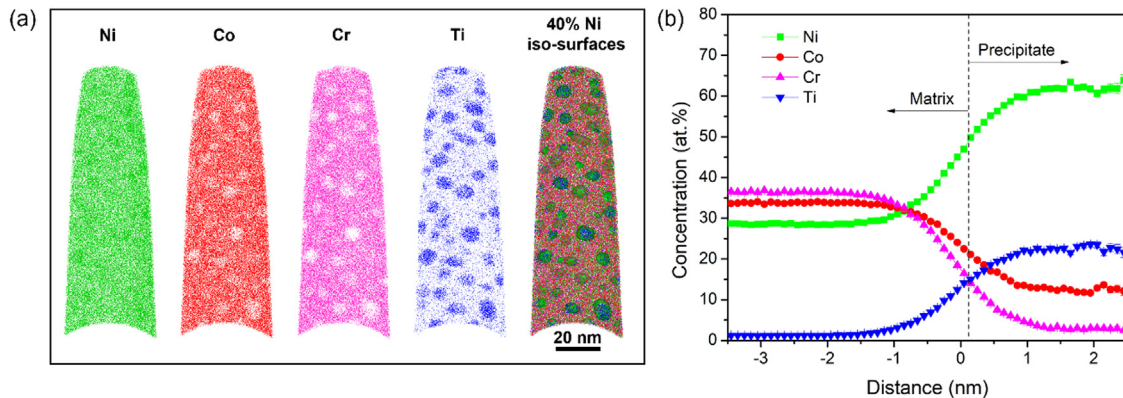


Fig. 13. (a) APT maps showing the distribution of spherical precipitates and (b) proximity histogram of concentration profiles for all elements across the matrix/precipitate interface in the NiCoCrTi_{0.1} MEA irradiated at 700 °C.

weaker lattice distortion and lower SFE, dislocation loops with smaller sizes while larger densities tend to form in FeCoNiCrMn during He irradiation at 350~450°C. The minor additions of W and Ti in NiCoCr give rise to different dislocation loop formation behaviors, even though both the two different alloying elements enhance the lattice distortion degree of the alloy due to their larger atomic radii than the principal elements. This can be attributed to the significantly different SFEs of the two NiCoCr-based MEAs.

In comparison with NiCoCr, the increased SFE in NiCoCrW_{0.1} energetically decreases the formation driving force of Frank loops and then suppresses their growth. For the NiCoCrTi_{0.1} MEA, the effect of decreased SFE is suggested to overwhelm that of the enhanced lattice distortion and assist the growth of dislocation loops.

On the other hand, during He irradiation at 400°C, the implanted He atoms accumulate with survived vacancies to form spherical He bubbles due to the balance between the surface en-

ergy and bubble pressure [37]. Generally, the growth of He bubbles is determined by the He diffusivity, which is closely related to the diffusivities and concentrations of vacancies [13,37]. Previous studies have reported that at temperatures below $0.5T_m$ of HEAs, He bubble growth can be delayed in materials with more principal elemental constituents, mainly attributed to the hindered vacancy mobility and enhanced defect recombination due to the stronger compositional complexity [10,16,24]. This is identical to the current results, i.e., FeCoNiCr displays smaller He bubbles than the NiCoCr-based MEAs. Alike the variability of dislocation loops, the enhanced lattice distortion and the potential sluggish diffusivity of W atoms delay the vacancy diffusion of the W-alloyed NiCoCr MEA, thus inhibiting He bubble growth and resulting in the formation of smaller He bubbles. Meanwhile, our previous study revealed the introduction of minor Ti elements in FeCoNiCr could reduce the vacancy migration energy, thus facilitating the He bubble growth [38]. It is suggested that Ti-doping could also accelerate the vacancy diffusivity of NiCoCr, resulting in promoted He bubble growth behavior in the NiCoCrTi_{0.1} MEA.

In the He-irradiated materials at 400°C, the hardening increment is mainly attributed to the hindered dislocation mobility induced by dislocation loops and He bubbles. Generally, dislocation loops are regarded as strong obstacles, while He bubbles with small sizes can be considered weak obstacles [39,40]. Among the dislocation loops, Frank loops are the dominant contributors to radiation hardening due to their immobile nature. It has been reported that with the increasing chemical complexity in HEAs, the incubation period of dislocation loops tends to be delayed during irradiation, leading to the formation of faulted loops with a higher fraction [11]. Meanwhile, the previous study revealed that after irradiation at 350–450°C, a larger fraction of faulted loops were formed in FeCoNiCrMn compared to Fe₅₀Mn₃₀Co₁₀Cr₁₀, indicating that compositional complexity plays a more significant role in stabilizing the faulted loops at the low-temperature regime [16]. Therefore, it is reasonable to deduce that a reduced proportion of faulted loops tends to form in NiCoCr with lower compositional complexity, resulting in mitigated irradiation hardening. The minor addition of W in NiCoCr increases the SFE of the alloy and promotes the unfaulting of Frank loops, then further reducing the fraction of faulted loops and alleviating the irradiation hardening. By comparison, the decreased SFE in the Ti-alloyed NiCoCr MEA should be responsible for the enhanced irradiation hardening behavior.

As the irradiation temperature elevated to 700°C, the prevalent dislocation lines in FeCoNiCr indicate that for the FeCoNiCr alloy, the current implantation temperatures lie within the stage wherein the dislocation loops are thermally unstable and then grow and interact with each other to produce a dislocation network. This result is consistent with the previous study [17]. In contrast, faulted dislocation structures can still be maintained in the NiCoCr-based HEAs. It is supposed that at 700°C which is higher than $0.5T_m$ for the studied alloys, remarkably promoted mobilities of point defects will give rise to indistinguishable defect recombination efficiencies in the materials. That means, the hindering functions of compositional complexity on the defect migration tend to become insignificant at high temperatures. Here, the relatively lower SFEs endow stronger thermal stability to interstitial-type faulted defects in the NiCoCr-based MEAs. This phenomenon is most significant in the NiCoCrTi_{0.1} alloy with an extraordinarily low SFE, which enables the further growth of faulted dislocation loops to extended stacking faults without unfaulting and dissociating.

Compared with FeCoNiCr, the NiCoCr-based MEAs with a lower degree of compositional complexity display stronger He-induced cavity growth resistance at 700°C. This is consistent with our previous results which demonstrated that stronger compositional complexity in HEAs can facilitate He cavity growth at high temper-

atures by accelerating preferential vacancy migration via oversized atoms [10]. Meanwhile, combining simulations and experiments, Shi et al. [41] demonstrated that the migration of interstitials tends to be confined in the Ti- and Zr-enriched regions in a refractory NbZrTi MEA during irradiation. The resultant suppressed long-range interstitial diffusion due to such chemical short-range order will significantly improve the recombination efficiency of point defects. In the current study, it is suggested that the minor addition of W and Ti elements in the NiCoCr MEA may promote the formation of chemical short-range order due to the potential strong clustering behavior of those refractory elements, thus enhancing the radiation resistance. However, further investigation is required to study the chemical short-range order in the NiCoCr-based MEAs. Among the studied alloys, NiCoCrTi_{0.1} display the strongest radiation resistance in terms of He cavity growth. In comparison to the other alloys, two striking contrasts of features can be observed in the 700°C-irradiated NiCoCrTi_{0.1} MEA, i.e., L₁₂ precipitates and extended stacking faults. It has been reported that the formation of nano-sized (~4 nm) clusters in a FeCoNiCrCu_{0.2} HEA during He⁺ irradiation can serve as trap sites for the He bubbles with similar sizes, thus suppressing their growth [38]. In the current study, the trapping effect of L₁₂ precipitates on He atoms and vacancies is suggested to be limited considering the much smaller sizes than the He cavities (i.e., ~24.2 nm) in the 700°C-irradiated NiCoCrTi_{0.1} MEA. As shown in Fig. 11d, most He cavities in NiCoCrTi_{0.1} are located on the stacking faults. Therefore, it is clear that the abundant stacking faults in the NiCoCrTi_{0.1} alloy can effectively trap He atoms and provide preferential nucleation sites for He cavity formation, which in turn inhibits the formation of deleterious He cavities with large sizes. This result is similar to a previous study in which the stacking faults in SiC can effectively suppress He bubble growth by modifying the energy landscape of point defects nearby the stacking faults [42]. It has been demonstrated that the introduction of high-density planar defects, such as interfaces in nanolayered composites and grain boundaries in nanocrystalline materials, can effectively suppress He bubble growth [43,44]. However, nanostructured materials are confronted with serious challenges at high temperatures due to their low thermal stability. To our knowledge, here we first demonstrate that the design of MEAs with low SFEs may have a more noteworthy impact due to the in-situ formation of extended stacking faults at high temperatures.

Conclusion

In summary, we have studied the He-induced radiation hardening at 400°C and cavity growth behavior at 700°C of FeCoNiCr and three NiCoCr-based MEAs, i.e., NiCoCr, NiCoCrW_{0.1} and NiCoCrTi_{0.1}. The lower compositional complexity of the NiCoCr-based MEAs not only brings about the formation of dislocation loops with lower densities at 400°C but also delays the preferential vacancy migration via oversized atoms at 700°C. Thus, compared with the typical FeCoNiCr alloy, the NiCoCr-based MEAs exhibited better radiation resistance in terms of both radiation hardening and He cavity growth. Among the NiCoCr-based MEAs, NiCoCrW_{0.1} displayed the best radiation hardening resistance due to its highest SFE and thus the lowest fraction of sessile Frank loops. Meanwhile, NiCoCrTi_{0.1} with the lowest SFE showed the strongest He cavity growth resistance, attributed to the in-situ formation of extended stacking faults which can serve as effective trap sites for He atoms and vacancies.

Declaration of Competing Interest

The authors declare that they have no known competing financial interests or personal relationships that could have appeared to influence the work reported in this paper.

CRediT authorship contribution statement

Shaofei Liu: Methodology, Data curation, Writing – original draft, Writing – review & editing. **Guma Yeli:** Supervision, Writing – review & editing. **Da Chen:** Methodology, Data curation. **Weitong Lin:** Methodology, Data curation. **Yilu Zhao:** Methodology, Data curation. **Junhua Luan:** Methodology, Data curation. **Shijun Zhao:** Data curation. **Tao Yang:** Data curation. **Ji-jung Kai:** Supervision, Project administration.

Data Availability

Data will be made available on request.

Acknowledgments

This work was financially supported by Hong Kong Research Grant Council (RGC) [Grant Nos. CityU 11205018, 11214820, 11209021, 9360161 and C1017-21G].

References

- [1] B. Cantor, I.T.H. Chang, P. Knight, A.J.B. Vincent, Microstructural development in equiatomic multicomponent alloys, *Mater. Sci. Eng. A* 375 (2004) 213–218.
- [2] B. Gludovatz, A. Hohenwarter, D. Catoor, E.H. Chang, E.P. George, R.O. Ritchie, A fracture-resistant high-entropy alloy for cryogenic applications, *Science* 345 (2014) 1153.
- [3] W. Kai, F.C. Chien, F.P. Cheng, R.T. Huang, J.J. Kai, C.T. Liu, The corrosion of an equimolar FeCoNiCrMn high-entropy alloy in various CO₂/CO mixed gases at 700 and 950 °C, *Corros. Sci.* 153 (2019) 150–161.
- [4] Z. Lei, X. Liu, Y. Wu, H. Wang, S. Jiang, S. Wang, X. Hui, Y. Wu, B. Gault, P. Konstis, D. Raabe, L. Gu, Q. Zhang, H. Chen, H. Wang, J. Liu, K. An, Q. Zeng, T.G. Nieh, Z. Lu, Enhanced strength and ductility in a high-entropy alloy via ordered oxygen complexes, *Nature* 563 (2018) 546–550.
- [5] H. Luo, Z. Li, A.M. Mingers, D. Raabe, Corrosion behavior of an equiatomic CoCrFeMnNi high-entropy alloy compared with 304 stainless steel in sulfuric acid solution, *Corros. Sci.* 134 (2018) 131–139.
- [6] J.W. Yeh, S.K. Chen, S.J. Lin, J.Y. Gan, T.S. Chin, T.T. Shun, C.H. Tsau, S.Y. Chang, Nanostructured high-entropy alloys with multiple principal elements: novel alloy design concepts and outcomes, *Adv. Eng. Mater.* 6 (2004) 299–303.
- [7] C. Lu, L. Niu, N. Chen, K. Jin, T. Yang, P. Xiu, Y. Zhang, F. Gao, H. Bei, S. Shi, M.R. He, I.M. Robertson, W.J. Weber, L. Wang, Enhancing radiation tolerance by controlling defect mobility and migration pathways in multicomponent single-phase alloys, *Nat. Commun.* 7 (2016) 13564.
- [8] Y. Zhang, G.M. Stocks, K. Jin, C. Lu, H. Bei, B.C. Sales, L. Wang, L.K. Beland, R.E. Stoller, G.D. Samolyuk, M. Caro, A. Caro, W.J. Weber, Influence of chemical disorder on energy dissipation and defect evolution in concentrated solid solution alloys, *Nat. Commun.* 6 (2015) 8736.
- [9] K. Jin, C. Lu, L.M. Wang, J. Qu, W.J. Weber, Y. Zhang, H. Bei, Effects of compositional complexity on the ion-irradiation induced swelling and hardening in Ni-containing equiatomic alloys, *Scr. Mater.* 119 (2016) 65–70.
- [10] S. Liu, W. Lin, D. Chen, B. Han, S. Zhao, F. He, H. Niu, J.-J. Kai, Effects of temperature on helium cavity evolution in single-phase concentrated solid-solution alloys, *J. Nucl. Mater.* 557 (2021) 153261.
- [11] C. Lu, T. Yang, K. Jin, N. Gao, P. Xiu, Y. Zhang, F. Gao, H. Bei, W.J. Weber, K. Sun, Y. Dong, L. Wang, Radiation-induced segregation on defect clusters in single-phase concentrated solid-solution alloys, *Acta Mater.* 127 (2017) 98–107.
- [12] Z. Zhang, D.E.J. Armstrong, P.S. Grant, The effects of irradiation on CrMnFeCoNi high-entropy alloy and its derivatives, *Prog. Mater. Sci.* 123 (2022) 100807.
- [13] G.S. Was, Fundamentals of Radiation Materials Science: Metals and Alloys, Springer, 2016.
- [14] S.J. Zinkle, J.T. Busby, Structural materials for fission & fusion energy, *Mater. Today* 12 (2009) 12–19.
- [15] S.J. Zinkle, L.L. Snead, Designing radiation resistance in materials for fusion energy, *Annu. Rev. Mater. Res.* 44 (2014) 241–267.
- [16] Z. Su, T. Shi, J. Yang, H. Shen, Z. Li, S. Wang, G. Ran, C. Lu, The effect of interstitial carbon atoms on defect evolution in high entropy alloys under helium irradiation, *Acta Mater.* 233 (2022) 117955.
- [17] Z. Fan, T.-n. Yang, B. Komabaiah, X. Wang, P.D. Edmondson, Y.N. Osetsky, K. Jin, C. Lu, H. Bei, L. Wang, K.L. More, W.J. Weber, Y. Zhang, From suppressed void growth to significant void swelling in NiCoFeCr complex concentrated solid-solution alloy, *Materialia* 9 (2020) 100603.
- [18] L.K. Mansur, W.A. Coglan, Mechanisms of helium interaction with radiation effects in metals and alloys: a review, *J. Nucl. Mater.* 119 (1983) 1–25.
- [19] E.E. Bloom, S.J. Zinkle, F.W. Wiffen, Materials to deliver the promise of fusion power – progress and challenges, *J. Nucl. Mater.* 329 (2004) 12–19.
- [20] B. Gludovatz, A. Hohenwarter, K.V. Thurston, H. Bei, Z. Wu, E.P. George, R.O. Ritchie, Exceptional damage-tolerance of a medium-entropy alloy CrCoNi at cryogenic temperatures, *Nat. Commun.* 7 (2016) 10602.
- [21] R.E. Stoller, M.B. Toloczko, G.S. Was, A.G. Certain, S. Dwarkanath, F.A. Garner, On the use of SRIM for computing radiation damage exposure, *Nucl. Instrum. Methods Phys. Res. Sect. B* 310 (2013) 75–80.
- [22] S.F. Liu, Y. Wu, H.T. Wang, J.Y. He, J.B. Liu, C.X. Chen, X.J. Liu, H. Wang, Z.P. Lu, Stacking fault energy of face-centered-cubic high entropy alloys, *Intermetallics* 93 (2018) 269–273.
- [23] S.F. Liu, Y. Wu, H.T. Wang, W.T. Lin, Y.Y. Shang, J.B. Liu, K. An, X.J. Liu, H. Wang, Z.P. Lu, Transformation-reinforced high-entropy alloys with superior mechanical properties via tailoring stacking fault energy, *J. Alloys Compds.* 792 (2019) 444–455.
- [24] D. Chen, Y. Tong, H. Li, J. Wang, Y.L. Zhao, A. Hu, J.J. Kai, Helium accumulation and bubble formation in FeCoNiCr alloy under high fluence He+ implantation, *J. Nucl. Mater.* 501 (2018) 208–216.
- [25] W.D. Nix, H. Gao, Indentation size effects in crystalline materials: a law for strain gradient plasticity, *J. Mech. Phys. Solids* 46 (1998) 411–425.
- [26] R. Kasada, Y. Takayama, K. Yabuuchi, A. Kimura, A new approach to evaluate irradiation hardening of ion-irradiated ferritic alloys by nano-indentation techniques, *Fusion Eng. Des.* 86 (2011) 2658–2661.
- [27] X. Liu, R. Wang, A. Ren, J. Jiang, C. Xu, P. Huang, W. Qian, Y. Wu, C. Zhang, Evaluation of radiation hardening in ion-irradiated Fe based alloys by nanoin-dentation, *J. Nucl. Mater.* 444 (2014) 1–6.
- [28] D. Chen, Y. Tong, J. Wang, B. Han, Y.L. Zhao, F. He, J.J. Kai, Microstructural response of He+ irradiated FeCoNiCrTi₂ high-entropy alloy, *J. Nucl. Mater.* 510 (2018) 187–192.
- [29] E. Aerts, P. Delavignette, R. Siems, S. Amelinckx, Stacking fault energy in silicon, *J. Appl. Phys.* 33 (1962) 3078–3080.
- [30] I. Povstugar, P.-P. Choi, S. Neumeier, A. Bauer, C.H. Zenk, M. Göken, D. Raabe, Elemental partitioning and mechanical properties of Ti- and Ta-containing Co-Al-W-base superalloys studied by atom probe tomography and nanoin-dentation, *Acta Mater.* 78 (2014) 78–85.
- [31] Y.L. Zhao, Y.R. Li, G.M. Yeli, J.H. Luan, S.F. Liu, W.T. Lin, D. Chen, X.J. Liu, J.J. Kai, C.T. Liu, T. Yang, Anomalous precipitate-size-dependent ductility in multicomponent high-entropy alloys with dense nanoscale precipitates, *Acta Mater.* 223 (2022) 117480.
- [32] X.H. Du, W.P. Li, H.T. Chang, T. Yang, G.S. Duan, B.L. Wu, J.C. Huang, F.R. Chen, C.T. Liu, W.S. Chuang, Y. Lu, M.L. Sui, E.W. Huang, Dual heterogeneous structures lead to ultrahigh strength and uniform ductility in a Co-Cr-Ni medium-entropy alloy, *Nat. Commun.* 11 (2020) 2390.
- [33] Z. Wu, H. Bei, G.M. Pharr, E.P. George, Temperature dependence of the mechanical properties of equiatomic solid solution alloys with face-centered cubic crystal structures, *Acta Mater.* 81 (2014) 428–441.
- [34] T.-n. Yang, C. Lu, G. Velisa, K. Jin, P. Xiu, M.L. Crespiello, Y. Zhang, H. Bei, L. Wang, Effect of alloying elements on defect evolution in Ni-20X binary alloys, *Acta Mater.* 151 (2018) 159–168.
- [35] Y. Zhang, S. Zhao, W.J. Weber, K. Nordlund, F. Granberg, F. Djurabekova, Atomic-level heterogeneity and defect dynamics in concentrated solid-solution alloys, *Curr. Opin. Solid State Mater. Sci.* 21 (2017) 221–237.
- [36] X.-X. Wang, L.-L. Niu, S. Wang, Energetics analysis of interstitial loops in single-phase concentrated solid-solution alloys, *J. Nucl. Mater.* 501 (2018) 94–103.
- [37] H. Trinkaus, B.N. Singh, Helium accumulation in metals during irradiation – where do we stand? *J. Nucl. Mater.* 323 (2003) 229–242.
- [38] D. Chen, S. Zhao, J. Sun, P. Tai, Y. Sheng, G. Yeli, Y. Zhao, S. Liu, W. Lin, W. Kai, J.-J. Kai, Effects of minor alloying addition on He bubble formation in the irradiated FeCoNiCr-based high-entropy alloys, *J. Nucl. Mater.* 542 (2020) 152458.
- [39] C. Fan, Q. Li, J. Ding, Y. Liang, Z. Shang, J. Li, R. Su, J. Cho, D. Chen, Y. Wang, J. Wang, H. Wang, X. Zhang, Helium irradiation induced ultra-high strength nanotwinned Cu with nanovoids, *Acta Mater.* 177 (2019) 107–120.
- [40] E.G. Fu, A. Misra, H. Wang, L. Shao, X. Zhang, Interface enabled defects reduction in helium ion irradiated Cu/V nanolayers, *J. Nucl. Mater.* 407 (2010) 178–188.
- [41] T. Shi, Z. Su, J. Li, C. Liu, J. Yang, X. He, D. Yun, Q. Peng, C. Lu, Distinct point defect behaviours in body-centered cubic medium-entropy alloy NbZrTi induced by severe lattice distortion, *Acta Mater.* 229 (2022) 117806.
- [42] B. Li, H. Liu, T. Shen, L. Xu, J. Wang, F. Zhao, D. Peng, J. Li, Y. Sheng, A. Xiong, Irradiation-induced microstructure damage in He-irradiated 3C-SiC at 1000°C, *J. Eur. Ceram. Soc.* 40 (2020) 1014–1022.
- [43] W.Z. Han, N.A. Mara, Y.Q. Wang, A. Misra, M.J. Demkowicz, He implantation of bulk Cu-Nb nanocomposites fabricated by accumulated roll bonding, *J. Nucl. Mater.* 452 (2014) 57–60.
- [44] K.Y. Yu, Y. Liu, C. Sun, H. Wang, L. Shao, E.G. Fu, X. Zhang, Radiation damage in helium ion irradiated nanocrystalline Fe, *J. Nucl. Mater.* 425 (2012) 140–146.